A DEM study on the effect of chamber boundary on CPT calibration chamber tests

Abouzar Sadrekarimi[1#], and *Shayan* Hashemi[2]

[1]*Western University, Department of Civil & Environmental Engineering, London, Ontario, Canada*
[2]*SLR Consulting, Toronto, Ontario, Canada*
[#]*Corresponding author: asadrek@uwo.ca*

ABSTRACT

Laboratory-scale cone penetration tests are often carried out to calibrate the response of cone penetration, and in particular cone tip resistance to soil characteristics. However, because of the limited sample size, sample boundaries can often affect the measured cone resistance in laboratory tests. This paper presents numerical simulations using the discrete element method (DEM) to study the effect of boundary condition on cone penetration calibration chamber tests. Numerical simulations were performed under flexible (BC1) and laterally-constrained (BC3) boundary conditions on K_0-consolidated models at different relative densities and vertical stresses. Additional models were simulated with periodic boundaries (BC5) to model the free-field condition. To track the radial stress variations in different sections of the chamber, scattered representative volume elements (RVE) were embedded in the models. Particle displacements and contact force chains were examined to determine the relation between microscopic variables and macroscopic response of the specimens subjected to cone penetration under different boundary conditions. Larger cone resistances were obtained under BC3 condition than those in BC1 condition. For the chamber-to-cone diameter ratio of 25 adopted in this study, the influence of the lateral boundary was found to be negligible in loose to medium-dense assemblies, while the effect of chamber boundary amplified in dense to very dense samples with increasing relative density and reduced with increasing vertical stress. This was attributed to the higher radial stress induced along the cone penetration path in laterally-constraint BC3 models. Based on these findings, a correction factor is proposed to better estimate free-field penetration resistance from calibration chamber experiments.

Keywords: CPT calibration chamber test; boundary condition; discrete element method; cone penetration test.

1. Introduction

Due to the challenges associated with obtaining undisturbed cohesionless soil samples, in-situ testing stands out as the most practical approach for assessing granular soil deposits. The Cone Penetration Test (CPT) serves as a widely adopted in-situ geotechnical characterization tool due to its simplicity, excellent repeatability, and ability to provide continuous data along the penetration depth. While CPT doesn't directly measure soil properties, research has focused on developing empirical correlations between CPT measurements and engineering properties using laboratory calibration chamber experiments.

However, traditional calibration chamber tests with a standard cone pose challenges, requiring large-diameter chambers, making sample preparation time-consuming, and control over uniformity and external stresses challenging. To address this, researchers have explored reduced-scale calibration chambers and miniature cone penetrometers (Abedin 1995; Huang and Hsu 2005; Kumar and Raju 2009; Pournaghiazar et al. 2011). Yet, uncertainties arise from the sample boundary effect on measured cone penetration resistance.

Past studies have investigated the influence of boundary conditions on cone tip resistance (q_c) in calibration chamber tests, often assessing the effect based on the ratio of chamber (D_c) to cone (d_c) diameters, i.e., $R_d = D_c/d_c$, theoretically infinite in the field. Chamber boundary effects have been observed to increase (Bellotti 1984; Parkin 1988; Sisson 1990) or somewhat decrease (Bolton et al. 1999; Gui et al. 1998; Sisson 1990) q_c with rising R_d. Despite the significance of the chamber boundary on cone tip resistance, there have been limited studies utilizing discrete element modeling to examine this effect. This study utilizes numerical discrete element analyses of a specific CPT calibration chamber device designed at Western University (Damavandi and Sadrekarimi, 2015; Sadrekarimi and Jones, 2022) to examine the chamber boundary's impact. The study also analyses the influences of relative density and effective stress level on the chamber boundary effect.

2. Methodology

2.1. Model sand

This study employed PFC 3D (Itasca Consulting Group Inc.) to simulate DEM cone penetration tests. In the PFC simulation, soil grains were represented as spherical particles interacting at their contacts, utilizing the rolling resistance linear contact model. This model incorporates particle rolling resistance along with normal and tangential contact stiffnesses. Fig. 1 illustrates the scaled-up particle size distribution of a natural local sand

by a factor of 9 in the DEM models. Consequently, the median (D_{50}) and maximum (D_{max}) particle diameters increased from 0.845 mm and 0.234 mm in the natural sand to respectively 2.108 mm and 7.605 mm in the DEM model. Despite these changes, coefficients of uniformity (C_U) and curvature (C_C) remained constant, preserving the original shape of the gradation curve. The natural sand, following ASTM Standard procedures (ASTM 2014, 2016a, 2016b), exhibited a specific gravity (G_S) of 2.67, maximum (e_{max}), and minimum (e_{min}) void ratios of 0.845 and 0.525, respectively.
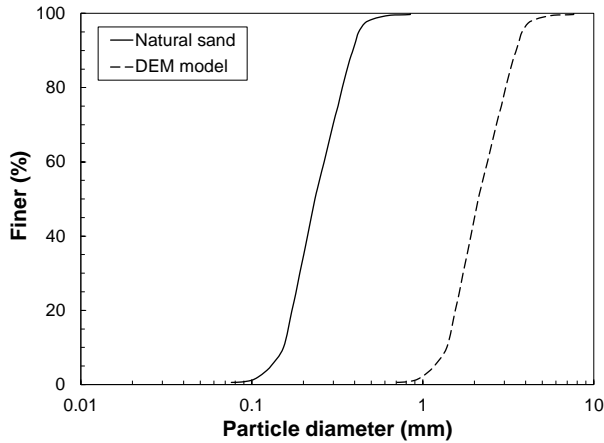
Figure 1. Particle size distributions of the natural sand and the scaled DEM model.

2.2. Parameter calibration

Five micromechanical parameters essential for conducting a DEM simulation with the rolling resistance linear contact model were determined and calibrated (Hashemi, 2021) based on the results of drained direct simple shear (DSS) and one-dimensional odometer tests (Mirbaha and Sadrekarimi 2017) conducted on the natural sand. For the DSS test modeling, assemblies with 20,000 spheres were generated. As illustrated in Fig. 2, these particle assemblies were confined by highly frictional unyielding plates on top and bottom, along with 10 rigid rings in peripheral positions. After iterative cycles to reduce particle overlaps, consolidation was achieved through the upper plate at σ'_{vc} values of 50, 300, and 400 kPa using a servo-mechanism. The resulting cylindrical sample dimensions matched those of the laboratory DSS tests (70 mm in diameter, 20 mm in height). Quasi-static shearing was applied by imposing a linearly increasing horizontal velocity on the confining rings. In drained shearing, the upper platen's servo-controlled mechanism maintained a constant σ'_{vc}. Stress-controlled odometer simulations followed a similar approach, utilizing a rigid frictionless cylinder for sample confinement in Fig. 2. The particle assembly, akin to the DSS model, underwent compression to varying σ'_{vc} levels (40 to 400 kPa) using a servomechanism on the upper plate. Void ratios (e_c) in both simulations were measured via representative volume elements (RVEs) embedded in the middle section of the samples. The calibrated modeling parameters are summarized in Table 1. A particle density of 2,690 kgf/m³, corresponding to the specific gravity of the Boler sand particles, was also used in the DEM simulations.
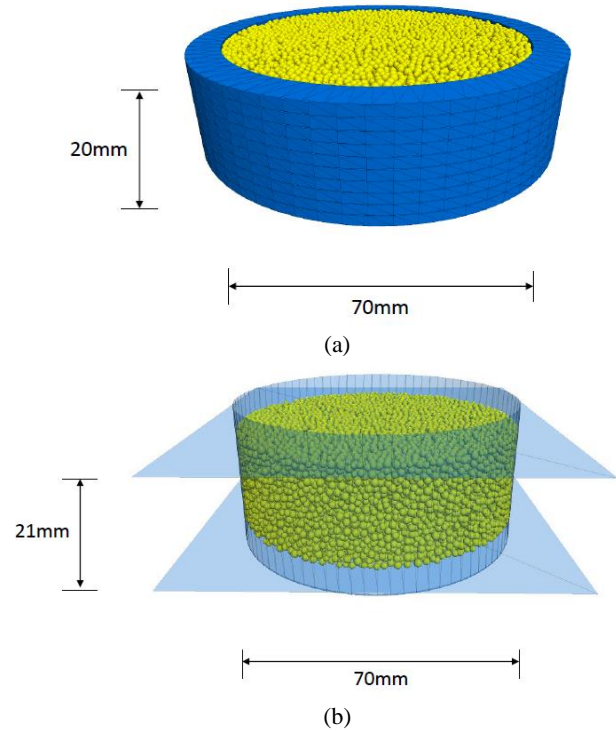

(a)

(b)

Figure 2. Schematics of the DEM-based (a) DSS and (b) odometer models of this study.

Table 1. Calibrated DEM parameters used in this study

| Microparameter	Value
Particle density (kgf/m³), ρ	2690
Contact elasticity modulus (MPa), E	100
Normal to shear contact stiffness, k_{ratio}	1.5
Inter-particle friction coefficient, μ	0.5
Inter-particle rolling coefficient, η	0.4
Non-local damping coefficient, α	0.1

2.3. Model preparation

For the DEM simulation of CPT, a three-dimensional (3D) axisymmetric cylindrical sample of 10.0 cm high (H) and 15.0 cm in diameter (D_c) was adopted. The model was subsequently filled with 180,000 particles and enclosed by two rigid boundaries at its top and bottom surfaces. CPT models were generated by initiating a cloud of randomly overlapping particles within the sample domain, allowing them to achieve equilibrium while minimizing overlap. Subsequently, the particles underwent settling under gravity, followed by the imposition of a specific boundary condition. For the constant stress boundary condition (BC1), stresses on the sample boundaries were controlled using a servo-controlled mechanism. The lateral stress was determined as $K_0\sigma'_{vc}$, with K_0 representing the lateral stress ratio established during sample consolidation under a laterally-confined condition. In the laterally constrained models (BC3), the sample was created within a rigid cylinder and subjected to σ'_{vc} through a servomechanism

at the bottom. A third set of simulations employed periodic boundaries to emulate infinite boundaries (as in field conditions), minimizing boundary effects in proximity to the cone. Throughout this paper, these simulations are denoted as BC5 conditions.

Samples with varying packing densities were created by adjusting the friction coefficient (μ) within the range of 0.05 to 0.5. The initial void ratios (e_c) of these models averaged at 0.757, 0.693, 0.636, and 0.570, determined through REV circles embedded within the simulated models. These corresponded to loose (relative density, $D_{rc} = 27\%$), medium-dense (relative density, $D_{rc} = 47\%$), dense (relative density, $D_{rc} = 65\%$), and very dense (relative density, $D_{rc} = 86\%$) assemblies, based on $e_{min} = 0.525$ and $e_{max} = 0.845$ of the natural sand. After consolidation and sample formation, the values of μ and η were reset to their calibrated values as indicated in Table 1.

2.4. Cone penetration

The simulated cone penetrometer included a lower sleeve with a frictional cylindrical wall, an upper sleeve with a frictionless cylindrical wall, and a rigid cone featuring a 60° apex angle, $d_c = 6$ mm, and a height of 5.2 mm. Consequently, the DEM samples aligned with a $R_d = 25$, mirroring the conditions of laboratory-scale CPT calibration chamber tests conducted at Western University (Damavandi-Monfared and Sadrekarimi 2015; Ganguly 2019; Sadrekarimi and Jones 2022). As depicted in Fig. 3, the cone was initially positioned at the top surface of the DEM model before penetration. Subsequently, the cone was pushed into the sample at a constant velocity of 10 cm/s, reaching a depth of 6 cm. Various penetration rates exhibited no discernible effect on the macroscale cone resistances in the DEM simulations, leading to the selection of a higher penetration rate (10 cm/s), compared to the 2 cm/s specified by the ASTM (2020) standard procedure, to optimize computational efficiency.
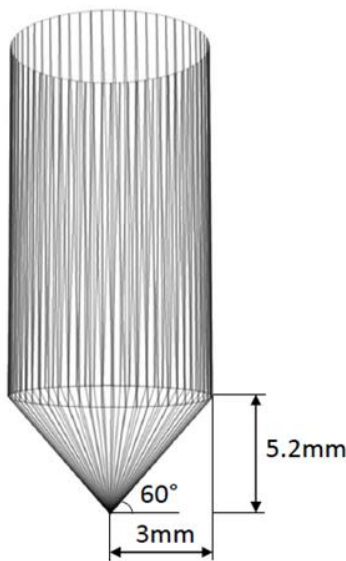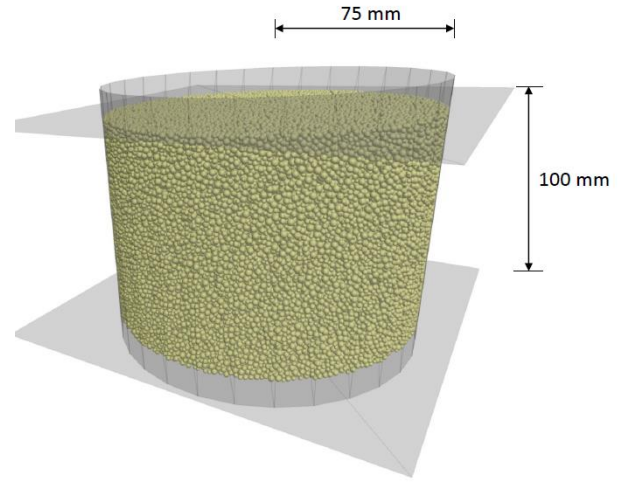

(b)

Figure 3. Schematics of the (a) cone penetrometer and (b) the cylindrical sample modeled in the DEM simulations of this study.

3. Results and Discussion

3.1. CPT profiles

Fig. 4 illustrates q_c profiles with cone penetration depth for different e_c and boundary conditions, focusing on simulations at $\sigma'_{vc} = 100$ kPa for brevity. Regardless of the boundary condition, q_c increased as e_c decreased (indicating densification) and with increasing penetration depth. Despite some fluctuations due to the scaled-up gradation in the CPT models, an average plateau was observed after reaching a penetration depth of approximately 4 cm in all simulations. In these simulations, q_c stabilized at deeper penetration depths in denser samples, requiring greater displacements to exhaust their higher dilatancy. Consequently, q_c values from penetration depths of 4 to 6 cm were averaged and considered the ultimate q_c mobilized in each DEM simulation, serving as a basis for various comparisons in subsequent sections.
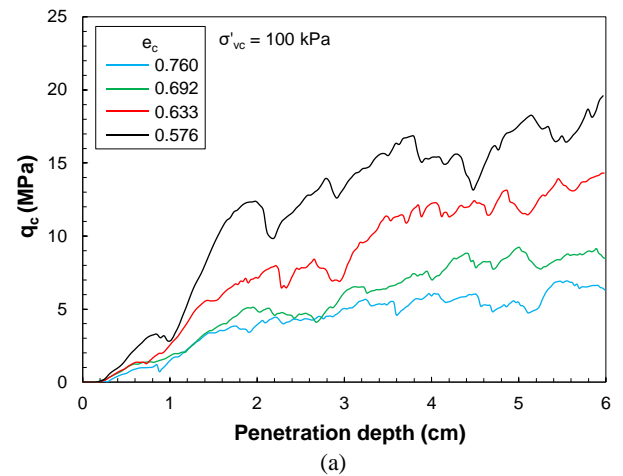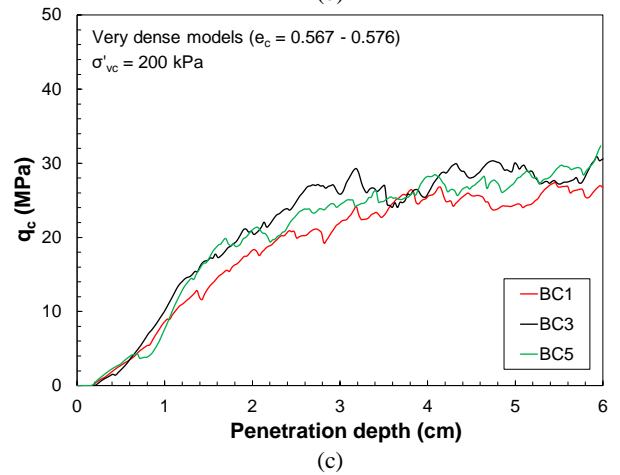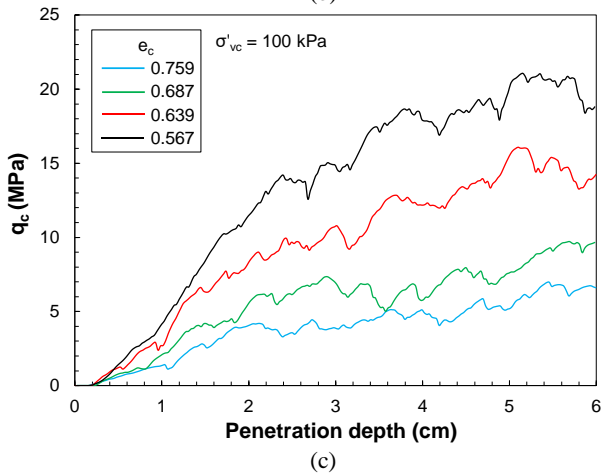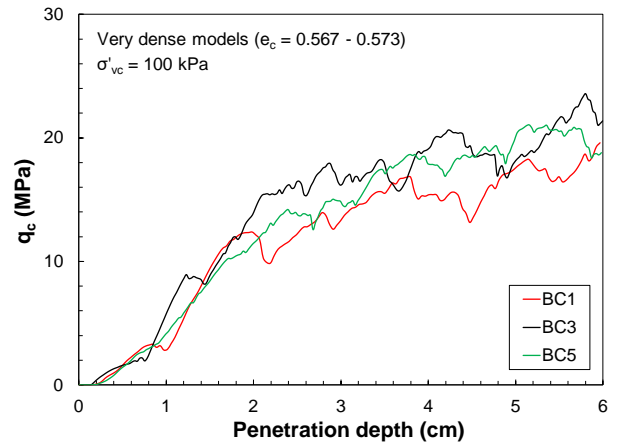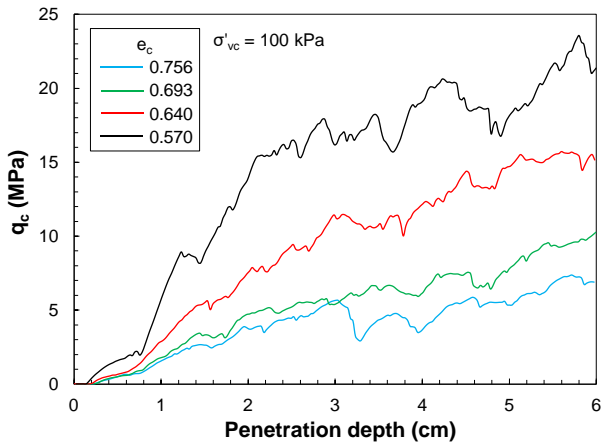

(a)

Figure 4. Profiles of q_c under a) BC1, b) BC3, and c) BC5 boundary conditions in loose, medium-dense, dense, and very dense samples at $\sigma'_{vc} = 100$ kPa.

3.2. Boundary effect

To emphasize the impact of the radial boundary condition, Fig. 5 juxtaposes q_c profiles for BC1, BC3, and BC5 boundary conditions in very dense samples ($e_c = 0.578 – 0.563$). Notably, BC3 exhibited comparatively higher q_c values than those observed under a BC1 boundary. Cone tip resistances in models featuring periodic boundaries (BC5) fell between values seen in BC3 and BC1 conditions, yet closely resembled those with the unyielding BC3 boundary. As depicted in Fig. 5, the influence of sample boundary condition on q_c appears to exhibit variability with σ'_{vc}.
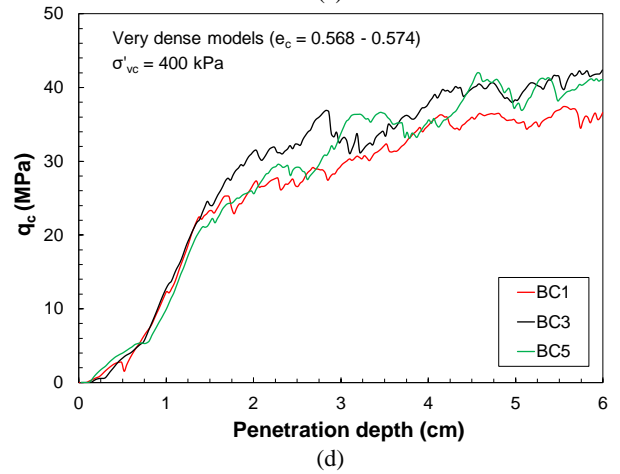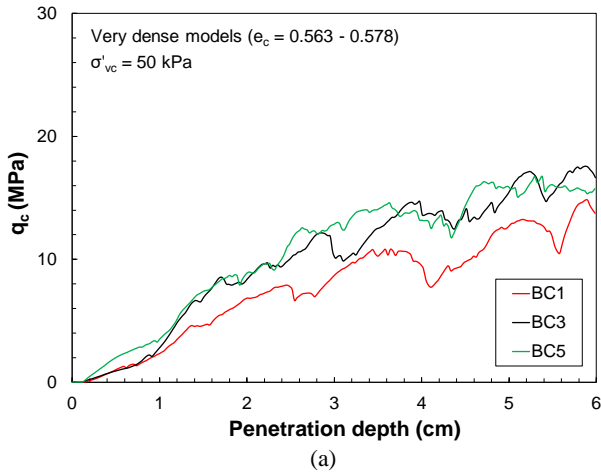

Figure 5. Effect of boundary condition on q_c in very dense DEM simulations for σ'_{vc} of a) 50 kPa, b) 100 kPa, c) 200 kPa, d) 400 kPa.
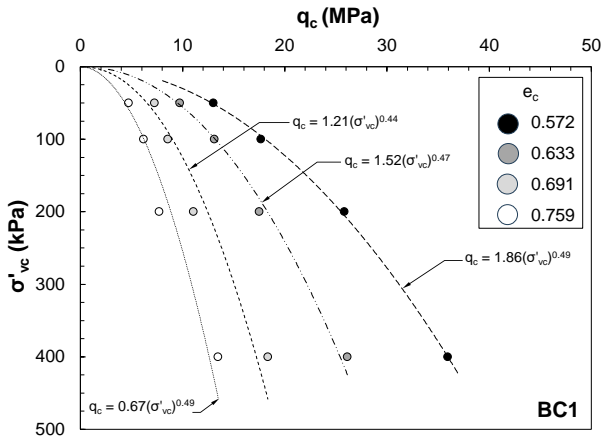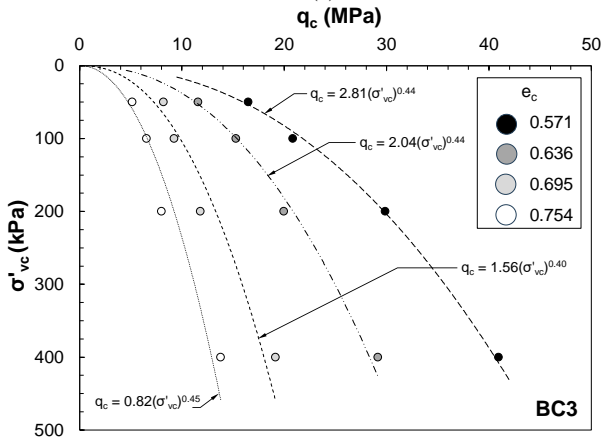
3.3. Effect of σ'_{vc}

Fig. 6 depicts the variations of q_c with overburden stress, σ'_{vc}, for each boundary condition based on the DEM simulations of this study. These are fitted with power functions for each e_c and boundary condition according to the following equation:

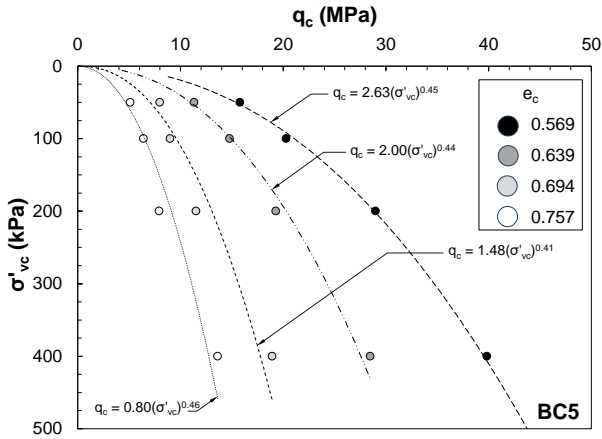$$q_c = q_{c1}(\sigma'_{vc})^n \qquad (1)$$

where, q_{c1} is the overburden stress-normalized cone tip resistance, and "n" is the overburden stress normalization exponents for q_c.

Figure 6. Effect of σ'_{vc} on q_c for (a) BC1, (b) BC3, and (c) BC5 boundary conditions based on the DEM simulations of this study.

3.4. Effect of void ratio

Utilizing the outcomes of DEM simulations, Fig. 7 illustrates the influence of e_c on q_{c1}, as determined by Eq. (1). The figure reveals the emergence of a boundary effect as e_c decreases. While average q_{c1} values remained nearly identical for all boundary conditions in loose samples ($e_c = 0.750 - 0.766$), divergence became apparent at lower e_c (< 0.75). Models subjected to BC3 and periodic boundary conditions exhibited essentially identical q_{c1} values, while lower q_{c1} values were observed in models confined by a constant-stress boundary condition (BC1). These trends are subsequently modeled with exponential functions.
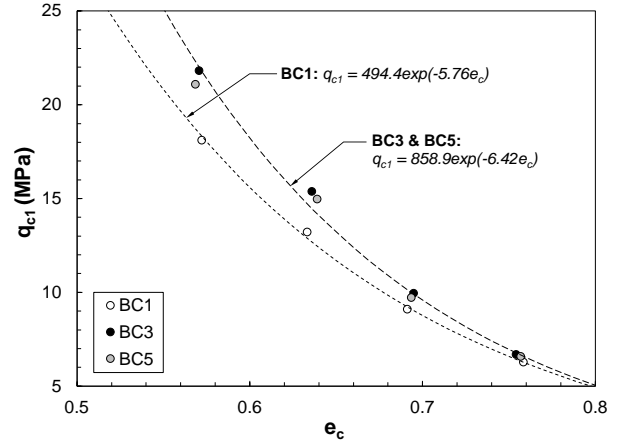

Figure 7. Effect of e_c on q_{c1} under different boundary conditions based on the DEM simulations of this study.

3.5. Radial stresses

The examination of boundary effects is extended by investigating the effective radial stresses (σ'_r) induced by each boundary condition along the penetrating cone path. These stresses were determined using multiple Representative Volume Elements (RVEs) embedded along the centerline of each model, each RVE comprising 1,500 particles within a radius of 10 mm ($20D_{50}$). Fig. 8 illustrates the variations in σ'_r/σ'_{vc} at penetration depths of 24 and 36 mm for samples subjected to $\sigma'_{vc} = 100$ kPa under different boundary conditions and e_c values. Within a specific boundary condition, σ'_r/σ'_{vc} generally decreased with decreasing e_c due to the enhanced frictional resistance in denser samples.

While similar σ'_r/σ'_{vc} values were observed for different boundaries in loose ($e_c = 0.760$) samples, the influence of the rigid radial boundary (BC3) became pronounced in medium-dense ($e_c = 0.687 - 0.693$), dense ($e_c = 0.633$), and very dense ($e_c = 0.567 - 0.573$) samples, exhibiting higher σ'_r/σ'_{vc} values than those in BC1 and BC5 boundary conditions. This resulted from the constraining effect of the unyielding BC3 boundary on the strong dilatancy behavior of dense and very dense samples. Consequently, the relatively larger q_{c1} mobilized with a BC3 boundary in Fig. 7 can be attributed to the comparatively higher σ'_r developed around the cone under this boundary condition. For a given e_c, σ'_r/σ'_{vc} values under BC5 condition also fell between those in models with BC1 and BC3 conditions.
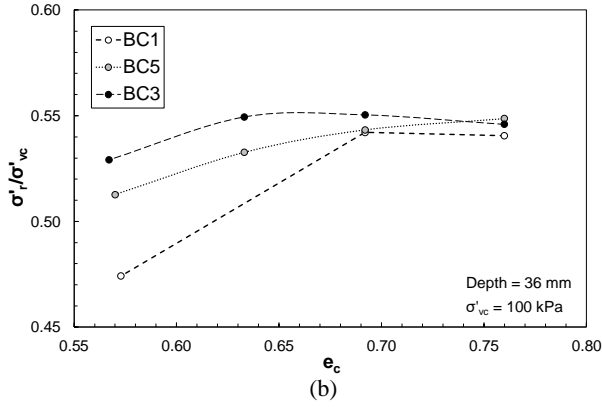
(b)
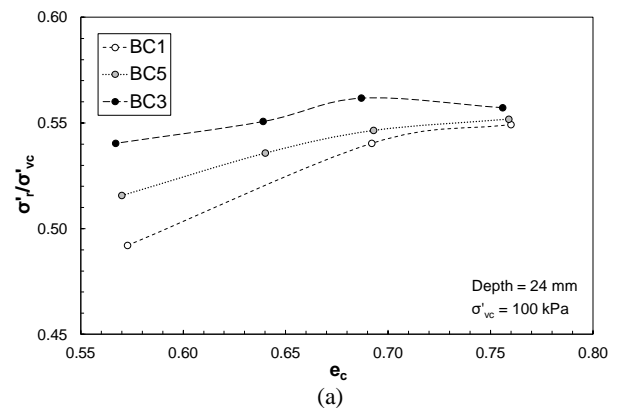
Figure 8. Changes of σ'_r/σ'_{vc} with e_c at penetration depths of (a) 24 mm and (b) 36 mm for different boundary conditions.

3.6. Interparticle forces and displacements

The positions and contact forces of particles were meticulously tracked and analyzed in Fig. 9, depicting interparticle force networks and particle displacement contours around the cone tip at the conclusion of cone penetration in very dense samples subjected to $\sigma'_{vc} = 100$ kPa. Line thickness in the force chain network corresponds proportionally to the magnitude of particle contact forces around the cone. As illustrated in Fig. 9, particle displacements and contact forces, indicative of the plastic behavior of the model, were primarily concentrated within a narrow zone surrounding the cone tip, gradually diminishing away from the cone. Furthermore, BC3 and BC5 conditions exhibit relatively stronger forces that extend farther from the cone compared to the BC1 model. The heightened interparticle forces prove more effective in displacing particles adjacent to the cone tip in simulations subjected to BC3 and BC5 conditions. Similar trends were observed in medium-dense and dense models exposed to varying σ'_{vc} values.
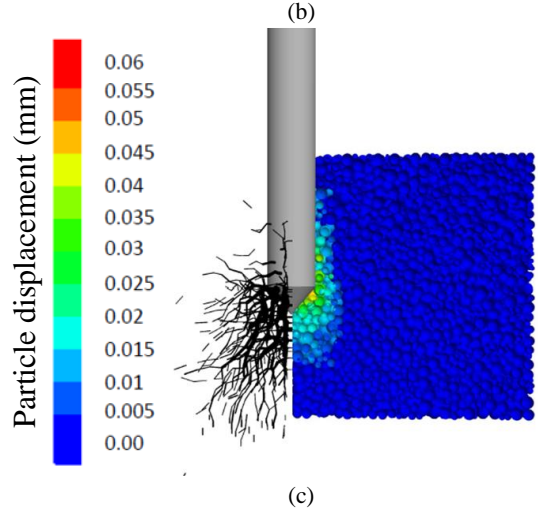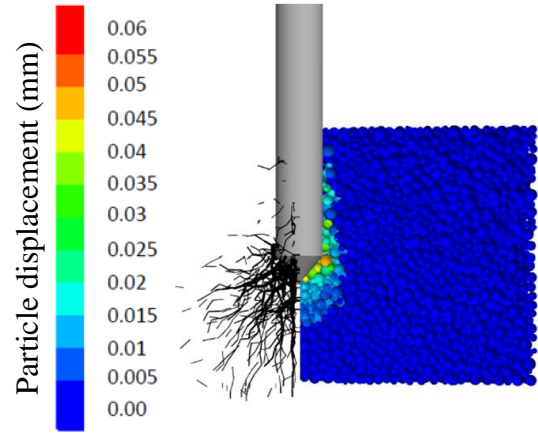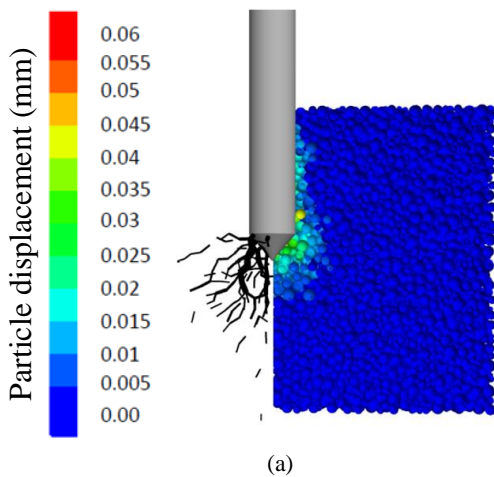

(a)

(b)

(c)

Figure 9. Distributions of strong forces and particle displacement contours at the end of penetration in very dense assemblies ($\sigma'_{vc} = 100$ kPa) under (a) BC1, (b) BC3, and (c) BC5 boundary conditions.

4. Boundary correct factor

Using simulations with the periodic boundary as the reference field-simulated condition, a correction factor (C_F) is proposed below to convert q_c from BC1 and BC3 conditions to the corresponding field value for a given overburden stress and density condition:

$$C_F = \frac{q_{c,f}}{q_{c,b}} \quad (2)$$

where $q_{c,f}$ and $q_{c,b}$ are cone tip resistances corresponding to BC5 (i.e., field condition) and BC1 (or BC3) boundary conditions, respectively. Fig. 10 illustrates the proposed correction factor with changes of σ'_{vc} for loose to very dense samples. Note that $C_F < 1$ and $C_F > 1$ represent respectively higher and lower $q_{c,b}$ values from the reference (i.e., periodic boundary) condition. While $C_F \approx 1$ for the BC3 boundary condition (indicating minimal effect), those corresponding to the BC1 boundary are not only higher in denser samples but also exhibit a notable reduction with increasing σ'_{vc}. This reduction could be attributed to the suppressed dilatancy and more contractive behavior of models at higher stress levels, as the chamber boundary effect primarily depends on sample dilatancy (Been et al. 1987).

Calibration chamber tests on loose to medium-dense sands and those conducted with a rigid boundary would closely approximate the field condition and require

minimal compensation for the limited effect of chamber size. Changes in q_c with different boundary conditions and the proposed C_F values are anticipated to decrease at higher R_d values than $R_d = 25$ adopted in this study. The effect of chamber boundary and the correction magnitude may also vary among different sands based on their compressibility (Jamiolkowski et al. 2001; Sisson 1990).
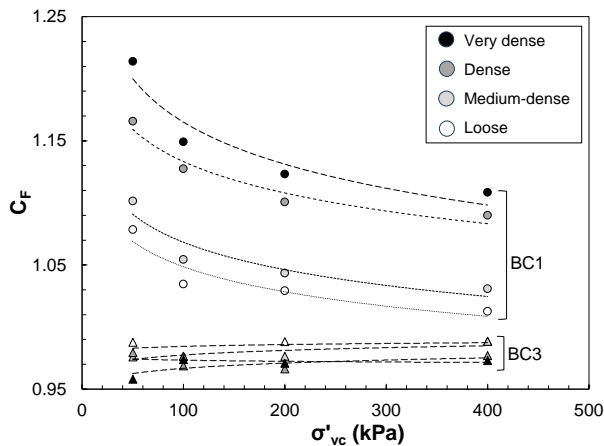

Figure 10. Chamber boundary correction factors established based on the DEM simulations of this study for BC1 and BC3 boundary conditions.

5. Conclusions

The study delved into the influences of constant stress (BC1) and zero-strain (BC3) lateral boundary conditions on cone tip resistance and sleeve friction through 3D numerical DEM simulations conducted on a clean silica sand. Results from the numerical models indicated minimal boundary effects in loose and medium-dense samples but pronounced effects in dense and very dense samples. Particularly in dense conditions, the rigid unyielding boundary heightened interparticle contact forces and radial stress around the cone tip, resulting in elevated cone tip resistances compared to a deformable boundary. The field-simulated periodic boundary condition (BC5) exhibited similar cone tip resistances to those under BC3, implying that BC3 had a less significant impact on cone tip resistance than BC1. Consequently, traditional CPT calibration chamber tests with a flexible membrane (BC1) may not faithfully replicate field stress and boundary conditions. To address this, a correction factor based on DEM results was developed to adjust for the effect of boundary condition on cone tip resistance.

References

Abedin, M. Z. "The characterization of unsaturated soil behaviour from penetrometer performance and the critical state concept", PhD Thesis, Department of Civil Engineering and Geosciences, Newcastle University, 1995.

ASTM. "Standard D854: Standard test methods for specific gravity of soil solids by water pycnometer", Annual Book of ASTM Standards, ASTM International, West Conshohocken, PA, 2014.

ASTM. "Standard D4253: Standard test methods for maximum index density and unit weight of soils using a vibratory table", Annual Book of ASTM Standards, ASTM International, West Conshohocken, PA, 2016a.

ASTM. "Standard D4254: Standard test methods for minimum index density and unit weight of soils and calculation of relative density", Annual Book of ASTM Standards, ASTM International, West Conshohocken, PA, 2016b.

ASTM. "Standard D5778: Standard test method for electronic friction cone and piezocone penetration testing of soils", Annual Book of ASTM Standards, ASTM International, West Conshohocken, PA, 2020.

Been, K., M. G. Jefferies, J. H. A. Crooks, and L. Rothenburg. "The cone penetration test in sands. Part II, general inference of state", Geotechnique, 37(3), pp. 285 – 299, 1987.

Bellotti, R. "Chamber size effects and boundary condition effects", In: Seminar on Cone Penetration Testing in the Laboratory, Southampton, England, 1984.

Bolton, M. D., M. W. Gui, J. Garnier, J. F. Corte, G. Bagge, J. Laue, and R Renzi. "Centrifuge cone penetration tests in sand", Geotechnique, 49(4), pp. 543 – 552, 1999.

Damavandi-Monfared, S., and A. Sadrekarimi. "Development of a miniature cone penetrometer for calibration chamber testing", Geotech Test J, 38(6), pp. 878 – 892, 2015.

Ganguly, R. "Miniature cone penetration tests with shear wave velocity and electrical resistivity measurements in characterization of silica sand", MESc thesis, Department of Civil and Environmental Engineering, Western University, 2019.

Gui, M. W., M. D. Bolton, J. Garnier, J. F. Corte, G. Bagge, J. Laue, and R. Renzi. "Guidelines for cone penetration tests in sands", In: International Conference Centrifuge '98, Tokyo, Japan, 1998.

Hashemi, S. "Towards realistic simulation of penetration tests and instability analysis of sand: A micromechanical perspective", MESc Thesis, Western University, 2021.

Huang, A. B., and H. H. Hsu. "Cone penetration tests under simulated field conditions", Geotechnique, 55(5), pp. 345 – 354, 2005.

Jamiolkowski, M., D. C. F. Lo Presti, and M. Manassero. "Evaluation of relative density and shear strength of sands from CPT and DMT", In: Soil Behavior and Soft Ground Construction, ASCE Geotechnical Special Publication 119, American Society of Civil Engineers, Reston VA, USA, 2001, pp. 201 - 238.

Kumar, J., and K. V. S. B. Raju. "Miniature cone tip resistance of sand with fly ash using triaxial setup", Can Geotech J, 46(2), pp. 231-240, 2009.

Mirbaha, K., and A. Sadrekarimi. "Characterization of a carbonate sand based on shear wave velocity measurement", In: 3rd International Conference on Performance-based Design in Earthquake Geotechnical Engineering, Vancouver, Canada, 2017.

Parkin, A. K. "The calibration of cone penetrometers", In: First International Symposium on Penetration Testing, ISOPT-1, Orlando FL, USA, 1988.

Pournaghiazar, M., A. R. Russell, and N. Khalili. "Development of a new calibration chamber for conducting cone penetration tests in unsaturated soils", Can Geotech J, 48(2), pp. 314-321, 2011.

Sadrekarimi, A., and S. Jones. "Laboratory-scale seismic CPT calibration chamber tests on Fraser River sand", Can Geotech J, 59(8), 2022.

Sisson, R. C. "Lateral stresses on displacement penetrometers", PhD Dissertation, Department of Civil and Environmental Engineering, University of California, 1990.